

1 **Software defined radio decoding of DCF77: time and frequency**
2 **dissemination with a sound card**

3 **Jean-Michel Friedt¹ Clément Eustache², Émile Carry¹, Enrico Rubiola¹**

4 ¹FEMTO-ST Institute, Time & Frequency, CNRS-UBFC

5 ENSM, 26 rue de l'Épitaphe, 25000 Besançon, France

6 ²Master PICS, Université de Franche Comté, Besançon, France

7 **Key Points:**

- 8 • Software defined radio decoding of atomic-clock controlled very low frequency
9 signal
- 10 • Use of the phase modulation spectrum spreading for high resolution time of flight
11 measurement
- 12 • Ionosphere altitude variation measurement using a sound-card based setup

Abstract

We investigate time and frequency dissemination using Software Defined Radio processing of signals acquired from a Low Frequency emitter using a sound card. We use the resulting propagation time measurements for investigating some ionosphere physics and its interaction with cosmic ray flux. Rather than using the amplitude of the transmitted signal as classically considered, we here focus on a precise time of flight measurement by demodulating the spectrum spreading phase modulation added to the DCF77 amplitude modulation.

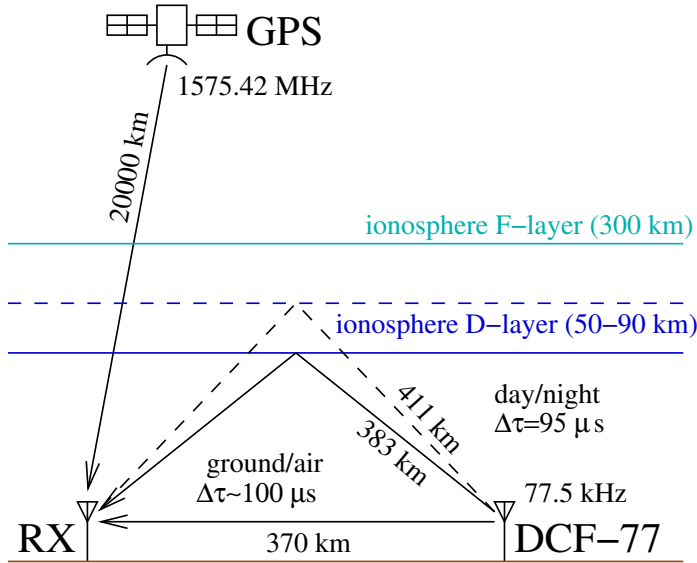
1 Introduction

Time and frequency dissemination has been an issue whenever a society aims at synchronizing activities (banking system, transports, power grid regulation) over a spatial range. Currently, Global Navigation Satellite Systems (GNSS) and the Global Position System (GPS) in particular, are amongst the reference time and frequency dissemination solutions exhibiting utmost stability, with accuracies ranging sub-100 ns when synchronizing a clock to the 1 PPS (Pulse Per Second) output of a GNSS receiver. However, these low power transmissions are prone to jamming and spoofing, so that alternative solutions are desirable. Low frequency (LF) solutions have been implemented well before the advent of GNSS [Watt *et al.*, 1972], and some emitters are still active, including the 77.5 kHz German DCF77 emitter located in Mainflingen (50°0'56"N, 9°00'39"E). This 50 kW emitter is powerful enough for its signal to be recovered over Western Europe [Bauch *et al.*, 2009; Piester *et al.*, 2011; Engeler, 2012], and the reader beyond this reach willing to decode its signal can collect records from websdr sites including <http://websdr.ewi.utwente.nl:8901/>. Most importantly for the physicist, the atomic clock-locked signal, with the reference signal provided by the German metrology laboratory PTB, interacts with the ionosphere, hence providing the means of probing ionosphere interactions with its environment [Baker and Lanzerotti, 2016], namely daily and seasonal cosmic ray flux fluctuations, and most significantly solar ionizing radiations. Such investigations have been classical since the 1960s [Blackband, 1964], but the proliferation of computers with huge computational power fitted with sound cards [Schulte *et al.*, 2012; Carlà, 2016] sampling at least at 192 ksamples/s allows for any curious experimenter to implement such a receiver at basically no cost since all demodulation schemes are implemented as software, the ultimate implementation of Software Defined Radio (SDR) princi-

45 ple in which the only hardware part is analog to digital conversion of the electromagnetic
46 signal reaching the antenna [*Kamp; Dolea et al.*, 2013]. Indeed, the current trend to shift
47 from analog to digital signal processing, especially in the context of time and frequency
48 metrology [*Uchino and Mochizuki*, 2004; *Mochizuki et al.*, 2007; *Gotoh et al.*, 2011; *Huang*
49 *et al.*, 2016; *Sherman and Jördens*, 2016], meets the requirements of improved stability,
50 flexibility and reconfigurability [*Mindell*, 2011] provided by SDR, which has become prac-
51 tical lately with the advent of radiofrequency high resolution analog to digital converters.

52 Ionosphere property fluctuations are linked to the cosmic ray flux variations. The
53 upper layers of the atmosphere are exposed to a flux of particles generated by the galac-
54 tic environment on the one hand, and the Sun on the other hand. The orientations of the
55 Earth with respect to this particle flux defines the ionosphere properties. Besançon, France
56 (47°N, 6°E), is located about 370 km from Mainflingen, so that a direct time of flight of
57 an electromagnetic wave lasts 1.2 ms. Assuming the same electromagnetic wave bounces
58 over the D-layer of the ionosphere located [*Blackband*, 1964; *Davies*, 1990; *Johler*, 1962]
59 at an altitude of about 50 km, the additional time delay is 100 μ s (Fig. 1). Furthermore,
60 assuming the ionosphere altitude varies from 50 to 90 km from day to night ionization
61 conditions – whether the Sun illuminates or not the upper atmosphere – an additional de-
62 lay of 95 μ s is expected: all these numbers result from basic geometric considerations of
63 straight paths between the emitter, the receiver and the reflector plane. Hence, investigat-
64 ing the ionosphere physics requires timing with sub-10 μ s accuracy if these effects are to
65 be observed.

71 Accurate timing requires some bandwidth spreading [*Raupach and Grosche*, 2014]
72 since time resolution is given as the inverse of the bandwidth of the incoming signal.
73 Such a requirement seems opposite to that of frequency dissemination which requires nar-
74 rowband signals. This dual need was originally met in the case of DCF77 with an ampli-
75 tude modulation once every second of an atomic-clock locked carrier, yielding timing ac-
76 curacy in the hundreds of microseconds due to the poor resolution of amplitude variation
77 detection. In the late 1980s an additional spread spectrum phase modulation scheme was
78 added allowing for much better timing accuracy [*Hetzel*, 1988]. Despite very few com-
79 mercial receivers using this additional mode – DCF77 receivers are fitted in most radio-
80 controlled clocks including low-cost weather stations – we will see that the tremendous
81 timing accuracy gain, over ten fold to reach sub-10 μ s accuracy, will allow us to address



66 **Figure 1.** Schematic of the LF signal propagation between Mainflingen (DCF77, Germany) and Besançon
 67 (RX, France), 370 km geodetic distance. The time of flight difference between the ground and air wave
 68 bouncing off the ionosphere is $100 \mu\text{s}$, and the ionosphere D-layer altitude variation between day and night in-
 69 duces another $95 \mu\text{s}$ delay in this geometric approximation. Ionospheric delay on the microwave GPS carrier
 70 is considered negligible in this application.

82 some of the ionosphere physics by processing the signal recorded by a personal computer
 83 sound card.

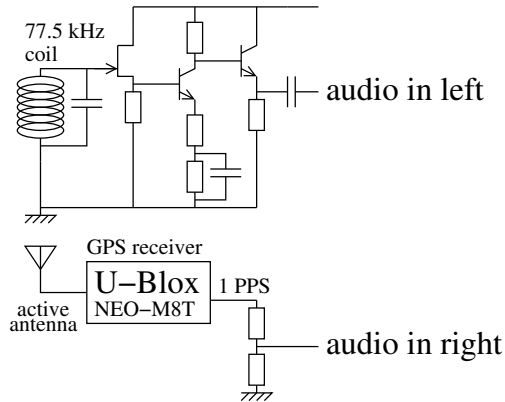
84 Based on these general considerations on long range wireless time transfer and the
 85 ability to probe ionospheric boundary conditions thanks to the high stability timing sig-
 86 nal, the outline of the paper is as follows. First, we will describe the hardware setup for
 87 receiving the radiofrequency signal using a common personal computer sound card: the
 88 hardware is limited to a bare minimum antenna impedance matching circuit, which nevethe-
 89 less requires some investigation considering the very short antenna dimensions with re-
 90 spect to the wavelength, its very high impedance and the need to buffer the signal before
 91 feeding the sound card. All demodulation and timing analysis are performed through soft-
 92 ware processing: implementation of the algorithms is developed in appendix A while the
 93 third section of the main text focuses on a description of the algorithm applied to extract
 94 first a stable phase and then a fine timing signal from the cross-correlation of the received
 95 signal phase with the known pseudo-random number sequence. Based on this analysis,
 96 the next section provides some measurement results demonstrating the timing accuracy is

97 sufficient to observe daily ionosphere altitude variations between daytime and night time,
98 as well as seasonal behaviour differences. Additionally, frequency stability measurements
99 allowing for local oscillator temperature induced drift are demonstrated. The core reason
100 for emitting timing signal over very low frequency signals being the long range synchro-
101 nization of quartz-controlled clocks, we develop the analysis needed to tune such a con-
102 trol loop. Finally the last section is devoted to a comparison of the vertical and horizontal
103 components of the electric field, representative of the two propagation paths through the
104 ionosphere and over ground of the very-low frequency signal. Throughout this investiga-
105 tion, the GPS 1-PPS signal is used as a reference with respect to which the DCF77 timing
106 signal is compared: a stereo sound card records simultaneously the two signals, hence re-
107 jecting the sound card clock impact on the measurement.

108 **2 Hardware setup**

109 SDR aims at limiting the hardware setup to an antenna connected to an analog to
110 digital converter. Most radiofrequency applications require however an additional mixing
111 step with a local oscillator since most analog digital converters (ADC) do not exhibit the
112 sampling rate – typically a few MHz – needed to sample radiofrequency signals: shifting
113 the signal under investigation from its carrier frequency to baseband, close to 0 Hz, also
114 allows for filtering strong interference sources and prevents saturating the sampling stage
115 with a wanted signal below the ADC resolution. VLF (Very Low Frequency, 3–30 kHz)
116 and LF (30–300 kHz) allow implementing true SDR receivers: meeting Nyquist criteria
117 of a sampling rate at least twice the targeted signal frequency range, recording DCF77
118 only requires an ADC with at least 150 ksamples/s sampling rate, a requirement met by
119 most current sound cards sampling at 192 ksamples/s. Alternatively, we have success-
120 fully used a Terrestrial Digital Video Broadcast (DVB-T) receiver fitted with a Realtek
121 RTL2832U analog to digital converter sending data on a USB bus, as implemented with
122 the Osmosdr GNURadio source, after removing the radiofrequency frontend: in such a
123 configuration, the in-phase (I) and quadrature (Q) inputs of the RTL2832U are respectively
124 connected to the DCF77 and GPS 1-PPS outputs, the latter as reference. GPS 1-PPS is
125 defined as a 1-Hz digital pulse whose rising edge matches, to within a few tens to a few
126 hundred nanoseconds depending on receiver technology and performance, the second of
127 the time disseminated by the GPS satellite constellation. In both cases, whether using the
128 sound card or the RTL2832U frontend, using dual-channel streams guarantees that the in-

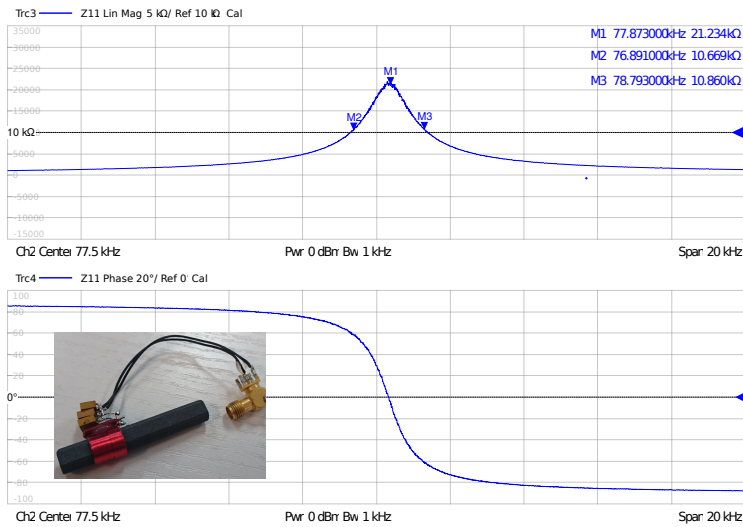
129 interleaved DCF77 and GPS measurements have been synchronously acquired. Since the
 130 electromagnetic signal emitted by DCF77 is vertically polarized, the coil antenna is, in
 131 this first setup, oriented horizontally with its normal pointing towards the emitter.



132 **Figure 2.** Schematic of the experimental setup: the coil receiving the DCF77 signal is tuned with a parallel
 133 capacitance for the antiresonance to match the targeted carrier frequency of 77.5 kHz. The high impedance
 134 output of the antenna feeds a FET transistor, for example BF245, before an amplifier and follower circuits
 135 based on NPN transistors, for example 2N2222, match the input impedance of one of the audio channels. The
 136 other audio channel is fed with an attenuated copy of the GPS receiver 1-PPS output as generated by a U-Blox
 137 Neo-M8T receiver.

138 Thus, we are able to connect an antenna straight to the sound card or RTL2832U
 139 input for further processing (Fig. 2): frequency shifting from LF band to baseband, fol-
 140 lowed by amplitude and phase demodulation. The only difficulty in setting up the an-
 141 antenna is the very long wavelength of the signal, meaning that the antenna is necessarily
 142 small [ARRL, 1997] with respect to the wavelength. Indeed, the 77.5 kHz of DCF77 has
 143 a wavelength of 3.8 km, so that a meter-long antenna will be considered infinitely small
 144 with respect to wavelength. It has been shown that such a small antenna necessarily ex-
 145 hibits high quality factor, a property usually frowned upon when designing an antenna
 146 aimed at operating over a wide frequency range, but here suitable since the antenna acts
 147 as a narrowband filter excluding strong nearby interferences, including switching power
 148 supplies and cathodic screens, and produces a strong voltage at the coil output. Further-
 149 more, such a sub-wavelength antenna exhibits a much larger impedance at anti-resonance
 150 than the sound card input: an impedance matching circuit feeding a high impedance input
 151 with the antenna coil current (FET transistor grid) and generating a low impedance out-

152 put is needed between the coil and sound card. Our circuit follows the inspiration from
 153 www.qsl.net/dl4yhf/dcf77_osc/index.html (accessed 2017), with the antenna scav-
 154 enged from the DCF77 receiver circuit sold by Conrad (product reference: 641138). It is
 155 worth noticing that strategies for designing such very small antennas differ significantly
 156 from resonant antenna design: while in the latter case the impedance is close enough to
 157 50Ω for the reflection scattering coefficient (S_{11}) to be representative of the efficiency
 158 of the antenna at a given wavelength, small antennas operating in an anti-resonant mode
 159 exhibit very high impedance, well above $10 \text{ k}\Omega$ (Fig. 3). Under such circumstances, mea-
 160 suring S_{11} will not allow for tuning the antenna operating frequency: either a conversion
 161 to admittance (real part) exhibits a maximum at anti-resonance where a maximum voltage
 162 is generated by a given current induced by a magnetic flux flowing through the loop an-
 163 tenna, or a transmission measurement in which a function generator induces, in a forced
 164 regime, a voltage at the output of the tuned antenna in a transmission mode measurement,
 165 will allow for tuning the capacitance connected in parallel to the inductor formed by the
 166 coil antenna to operate at the wanted frequency.



167 **Figure 3.** Coil antenna acting as an inductor, tuned to the operating frequency with a capacitor connected
 168 in parallel. Notice the maximum of the impedance at the operating frequency, as required to generate as
 169 high a voltage as possible for a given current induced by the magnetic flux flowing through the coil antenna.
 170 Both charts exhibit the impedance of the antenna as a function of frequency (linear scale), with the top figure
 171 displaying the magnitude and the bottom one the phase, in a frequency range of $77.5 \pm 10 \text{ kHz}$.

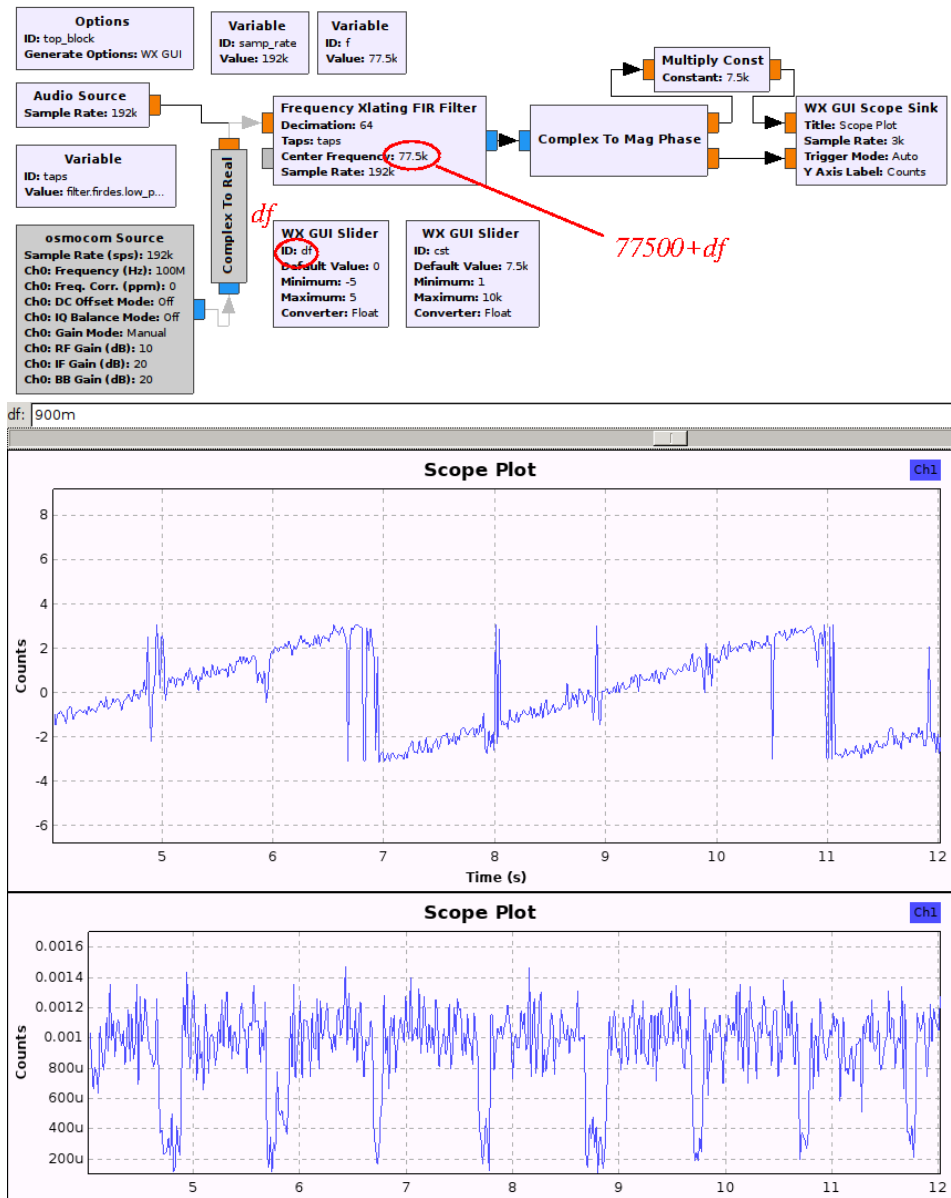
172 The initial prototyping steps have been performed using GNURadio, a software
 173 framework designed to help SDR enthusiasts prototype digital signal processing func-
 174 tionalities yet provide real time signal processing and visualization, as opposed to post-
 175 processing using Matlab or its opensource implementation, GNU/Octave. Phase detection
 176 and automated analysis over long durations will be performed with the latter software.
 177 Transposing from radiofrequency band to baseband is such a common SDR processing
 178 task that it is implemented as an optimized processing block in GNURadio (Fig. 4): the
 179 Xlating FIR Filter. The time t dependent signal $s(t)$ received at the antenna exhibits a sig-
 180 nal of interest modulated close to a carrier f_c , while recovering the property of the signal
 181 requires getting rid of the carrier: demodulating requires reproducing a local copy of f_c so
 182 that

$$s(t) \times \exp(j2\pi f_c t) \quad (1)$$

183 shifts the incoming signal to baseband (here $j^2 = -1$). Once the signal is shifted to base-
 184 band, the whole bandwidth, given by the initial sampling rate f_s , is no longer needed
 185 since the signal is band-limited: decimating, i.e. taking one in every N samples, reduces
 186 the bandwidth by a factor of N , easing processing steps since the datarate has been re-
 187 duced. However, decimating brings all signals in the initial frequency band of $[-f_s/2; +f_s/2]$
 188 to the new frequency band $[-f_s/(2N); +f_s/(2N)]$ by aliasing: low-pass filtering the fre-
 189 quency transposed signal prior to decimation is needed to get rid of these aliasing im-
 190 ages, hence the inclusion of the Finite Impulse Response (FIR) filter in the GNURadio
 191 processing block. We now have a signal at baseband whose information content, lying in
 192 the amplitude and phase, must be decoded: such task will be performed solely by software
 193 processing.

200 3 Frequency lock

201 Amplitude demodulation is a crude processing step exhibiting the poorest noise re-
 202 jection capability, but easiest to implement: the baseband signal is rectified and low-pass
 203 filtered. The local oscillator copy f_c only needs to be accurate enough for the signal to
 204 lie within the low-pass filter bandpass range. The narrower the low-pass filter the better
 205 the noise rejection, but also the longer the time response of the filter and hence the poorer
 206 the timing capability. We observe experimentally that a low-pass filter with 30 to 50 Hz
 207 bandwidth allows for observing the amplitude modulated pulses encoding time transfer,
 208 yielding time resolutions in the tens of millisecond. Practical amplitude pulse edge detec-



194 **Figure 4.** Top: GNURadio flowchart for realtime display of the decoded signal. The signal is sampled from
 195 a sound card (Audio Source), translated to baseband using the Xlating FIR Filter with a manually tunable
 196 frequency offset df with respect to the nominal 77500 Hz carrier frequency, and the phase and magnitude are
 197 displayed following low-pass filtering. Bottom: amplitude (bottom) and phase (top), with a slight frequency
 198 offset still visible as a linear phase drift over time. The amplitude modulated timing pulses are visible as
 199 signal drops every second on the bottom graph, with pulse width indicating the bit value.

209 tion shows that sub-millisecond time transfer is achieved using this strategy. Such a time

210 resolution is insufficient to detect ionosphere variations, which were demonstrated previ-
 211 ously to induce variations in the tens of microseconds range.

212 Pseudo-random phase modulation was introduced to spread the spectrum and im-
 213 prove timing resolution. The core aspect of this modulation scheme, also used in GNSS
 214 timing strategies with more complex implementations, is that the pseudo-random sequence
 215 is known, so that by cross-correlating a local copy of the code over the phase of the sig-
 216 nal transposed to baseband, a sharp cross correlation peak occurs when the two copies of
 217 the code are synchronized: the cross correlation peak width is given by the inverse of the
 218 bitrate, and the noise rejection capability of the cross correlation is given by the number
 219 of bits in the code. Indeed, the pseudo-random sequence exhibits a 0-mean value, so that
 220 noise is averaged by cross-correlating with the code, and only the appropriate sequence
 221 of phase values coherently accumulates energy in the cross-correlation peak. Depending
 222 on the signal to noise ratio, cross-correlation peak fitting provides an additional timing
 223 accuracy gain equal to the signal to noise ratio. The pseudo random code generator imple-
 224 mented in DCF77 is known: the 9-th degree polynomial function $x^9 + x^5 + 1$, whose imple-
 225 mentation in C language is given at [https://en.wikipedia.org/wiki/DCF77#Phase_](https://en.wikipedia.org/wiki/DCF77#Phase_modulation)
 226 [modulation](https://en.wikipedia.org/wiki/DCF77#Phase_modulation), feeds a linear feedback shift register generating a 511-bit long sequence
 227 with no repeating pattern over this duration, hence the spectrum spreading capability. The
 228 implementation informs us that the phase of the signal is updated every 120 periods of the
 229 DCF77 carrier, or at a rate of $77.5 \text{ kHz}/120 = 646 \text{ Hz}$. Hence the expected timing ac-
 230 curacy is in the 1.5 ms range with the improvement brought by the cross-correlation peak
 231 fitting, which yields an observed sub-10 μs accuracy.

232 The challenge of phase demodulation lies in reproducing a local copy of the unmod-
 233 ulated carrier in order to allow for phase variation detection. Indeed, frequency f being
 234 the derivate of the phase φ in the expression

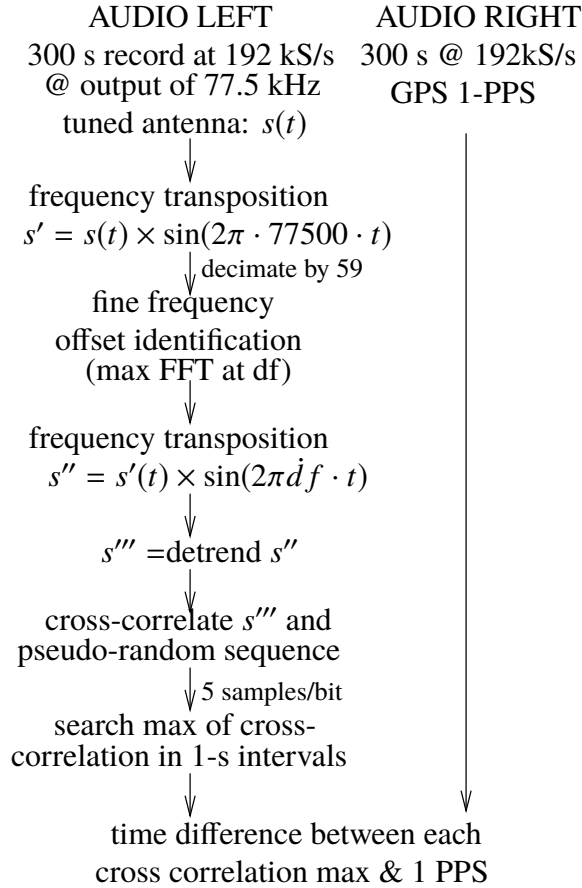
$$s(t) = \cos(2\pi ft + \varphi(t)) \quad (2)$$

235 the phase $\Phi = 2\pi ft + \varphi$ can be considered as split between a component linearly time
 236 varying with time $2\pi ft$ and a random component including the signal to be demodulated
 237 φ . Recovering φ hence requires an accurate estimate of f so that the mixing with the car-
 238 rier yielding $f - f_c$ cancels and only φ is left in the expression of Φ . While amplitude
 239 demodulation only requires that $f - f_c$ lies within the low-pass filter bandwidth, and no
 240 feedback control is usually implemented on f which is nominally close to f_c in ampli-

241 tude demodulation, phase demodulation requires f to track f_c to compensate for envi-
 242 ronmental fluctuations and oscillator aging of f , the local copy of f_c . A coarse approach
 243 is to bring the radiofrequency signal close to baseband by multiplying with the nominal
 244 value of $f_c = 77500$ Hz in our case, and then take the Fourier transform of the resulting
 245 complex signal. The abscissa δf of the maximum of the Fourier transform provides the
 246 frequency offset between f and its nominal value: the resulting signal is hence again mul-
 247 tiplied by $\exp(2\pi \delta f t)$ for the baseband to be centered on 0 Hz. Such a strategy is only
 248 as accurate as one Discrete Fourier transform bin, which is the decimated sampling rate
 249 divided by the number of samples of the Fourier transform. An improved frequency off-
 250 set estimation scheme is to perform a linear fit on the resulting phase, and compensate for
 251 any residual frequency offset by subtracting the linear trend. The latter processing step has
 252 been implemented but does not significantly improve our phase cross-correlation compu-
 253 tation capability. The general algorithm used to measure accurately the time of flight of
 254 the DCF77 signal with respect to the reference GPS 1-PPS signal is summarized in Fig.
 255 5. The practical implementation of these algorithm steps are given in appendix A.

262 However, this carrier frequency tracking solution already provides one result on fre-
 263 quency transfer: the sound card local oscillator will be affected by local environmental
 264 variations, most significantly temperature variations, readily observed with respect to the
 265 reference atomic clock signal received from DCF77. Plotting the frequency correction as
 266 a function of time – all records are timestamped with respect to Coordinated Universal
 267 time (UTC) – and comparing with the temperature history in Besançon (as provided by
 268 the local airport METAR logs provided at <https://www.wunderground.com/history/airport/LFSA/>), a clear correlation is observed (Fig. 6), as expected from the poor ther-
 269 mal insulation of the laboratory in which this experiment is taking place. The frequency
 270 offset of 0.8 Hz at 77500 Hz indicates a 10 ppm offset, with a temperature dependence of
 271 ± 0.5 Hz for temperature variations of $\pm 10^\circ\text{C}$, or a 0.6 ppm/K temperature dependence, a
 272 reasonable value for a quartz oscillator operating close but below its turnover temperature.
 273

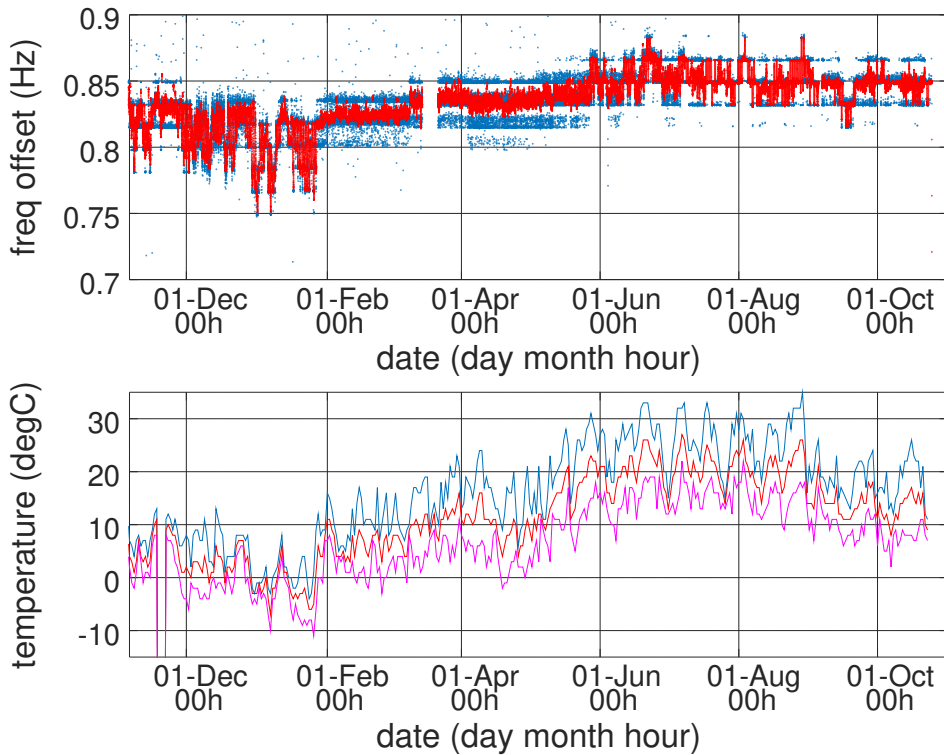
280 We have completed the frequency transfer investigation. However, observing iono-
 281 sphere altitude fluctuation requires solving the time transfer issue, which is addressed in
 282 the next section.



256 **Figure 5.** Processing steps applied to 60-second long measurement sequences of the DCF77 signal and
 257 the GPS-1PPS signal. Both signals are sampled with the stereo channels of a sound card clocked by the same
 258 reference signal, which is thus rejected when comparing one signal with respect to the other. Detrending
 259 involves identifying the linear trend on the dataset and removing this linear drift component. The decimation
 260 factor of 59 was selected for the decimated sampling rate of 192/59 kHz to closely match a small integer
 261 number of samples in the duration of one bit, namely 5 samples/bit as explained in the text.

283 4 Timing analysis

284 Having shifted the frequency to a baseband centered on 0, the phase $\Phi = \varphi(t)$ only
 285 exhibits variations introduced by the phase modulation scheme. Reproducing this sequence
 286 locally, and resampling so that an appropriate number of phase values match the dura-
 287 tion of each sampled bit, a cross-correlation of both signal yields sharp cross-correlation
 288 peaks once every second (Fig. 7). The GNU/Octave listing given in appendix A exhibits
 289 the core processing steps and illustrates a typical processing chain implementing as soft-
 290 ware the most common components found in a typical radiofrequency receiver, including



274 **Figure 6.** Top: frequency offset between the nominal received frequency of 77500 Hz, and the correc-
 275 tion brought to bring the LF signal to a baseband centered on 0 Hz. The red curve is a sliding average over
 276 10 samples (50 minute integration time) of the raw data shown in blue (each blue dot is the result of process-
 277 ing 60 second acquisitions). Bottom: history of the daily average of the temperature of Besançon airfield in
 278 Thise (METAR logs of LFSA callsign). The red curve is the mean daily temperature value recorded at the
 279 airfield, blue is the maximum and magenta is the minimum tempature recorded during each day.

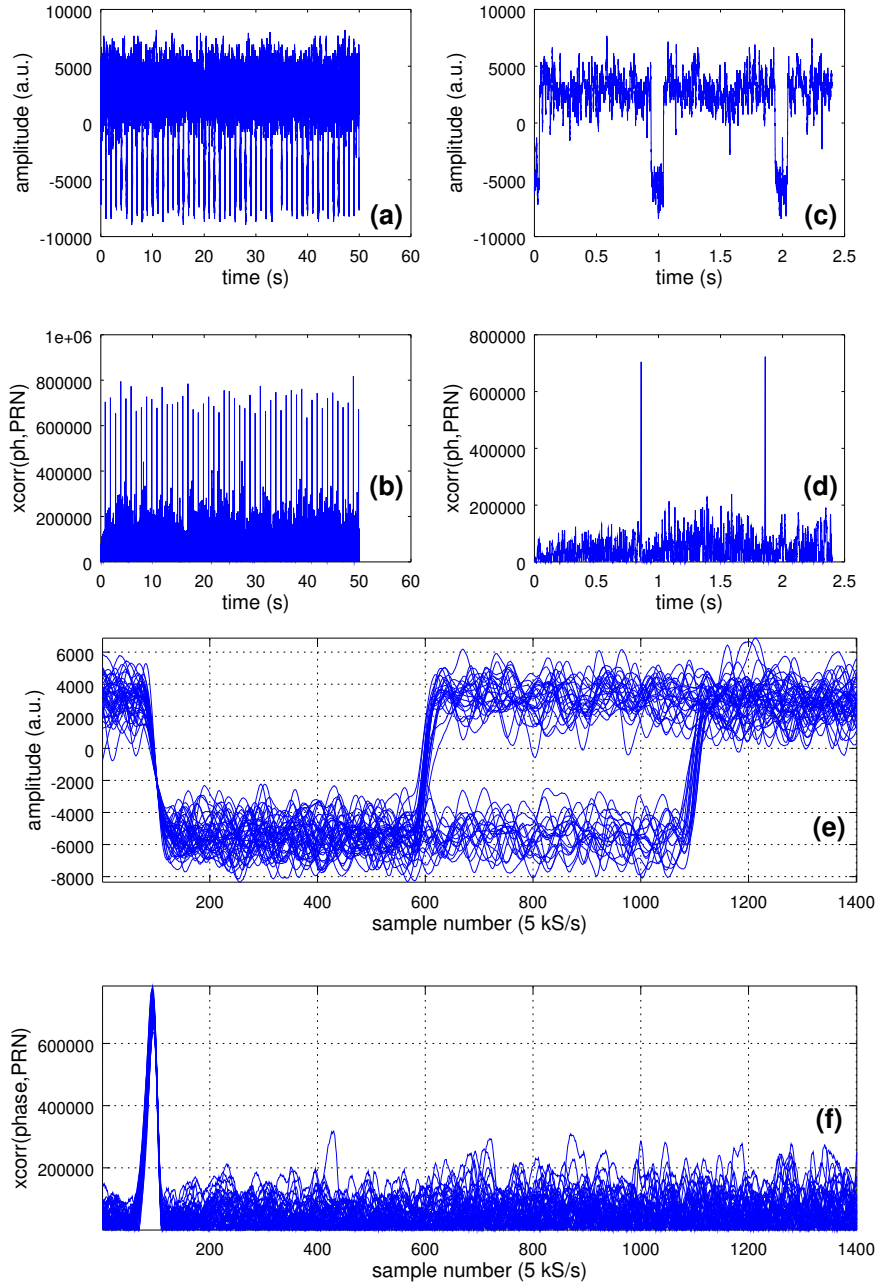
291 mixing, low-pass filtering, remote oscillator frequency tracking by the local oscillator (i.e.
 292 demodulation), and signal decoding. A first coarse frequency offset between the received
 293 signal and the local oscillator is estimated from the position of the Fourier transform max-
 294 imum. From this offset, a local oscillator signal is generated using a time signal synthe-
 295 sized with steps equal to the inverse of the sampling rate, and a dot product simulates the
 296 multiplier component that would be used otherwise for frequency transposition. Having
 297 removed the coarse frequency offset, a linear fit on the phase removes the residual linear
 298 trend of the phase, also known as frequency offset (since the derivate of the phase is the
 299 instantaneous frequency). A pre-computed pseudo-random code sequence is loaded and
 300 re-sampled at the same rate as the data recorded by the sound card. Following all these

301 steps, the cross-correlation between the pseudo random sequence and the phase whose
 302 linear drift has been removed must exhibit a sharp peak once every second, when both
 303 patterns match.

304 The cross-correlation between the detrended phase and the pseudo-random sequence
 305 is computed, having previously removed the mean value of each signal to prevent a tri-
 306 angular baseline variation due to the integral over a constant offset: the cross-correlation
 307 exhibits maxima every time the pseudo-random pattern is met in the phase of the recorded
 308 signal, as seen on Fig. 7 (b) and (d). The improvement in the timing accuracy is empha-
 309 sized by comparing the amplitude modulation (Fig. 7 (a) and (c)) indicating the beginning
 310 of each second, with the phase cross-correlation peak (Fig. 7 (d)): amplitude modula-
 311 tion being prone to link budget fluctuations and not being locked on the carrier during
 312 the demodulation which only consists of a rectifying and low-pass filtering, a narrowband
 313 low-pass filter induces bit spreading and degrades the timing resolution. Nevertheless, the
 314 two possible widths on the amplitude modulation encoding the one and zero values (short
 315 and long pulse) are well observed (Fig. 7 (e)). On the other hand, the spectrum spreading
 316 introduced by the phase modulation narrows the cross-correlation peak, allowing for much
 317 better timing analysis (Fig. 7 (f)). The time resolution gain on the phase cross-correlation
 318 measurement is visible by observing the width of the cross-correlation peak rising edge
 319 with respect to the amplitude pulse rising edges, both signals being synchronized on the
 320 falling edge.

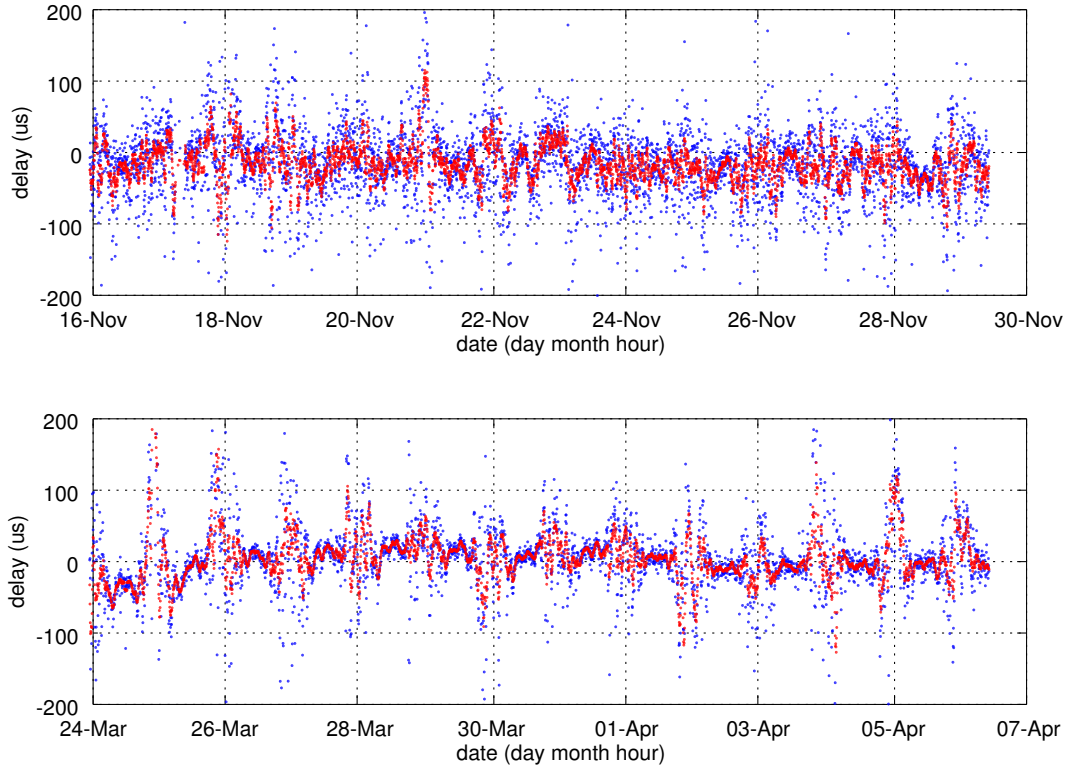
327 Estimating the accuracy of this decoding step requires a local copy of a timing sig-
 328 nal assumed to be a reference. We have compared the DCF77 cross-correlation peak tim-
 329 ing with the 1 PPS of GPS receivers designed for timing application: U-Blox (Switzer-
 330 land) provides low-cost (< 90 euros) GPS receivers with the timing option of the 1 PPS
 331 output. The sound card recording DCF77 is hence configured in stereo mode, with the
 332 second channel recording the GPS 1 PPS output.

339 Comparing the time of arrival of DCF77 and GPS, the latter assumed to be neg-
 340 ligibly affected by ionosphere delay in this configuration (sub-100 ns [*Giffard, 1999*]),
 341 yields a chart of time evolution exhibited in Fig. 8. The records are performed once every
 342 5 minutes, timestamped with the computer time set to UTC, with 1 minute long records
 343 requiring 4 to 5 minute processing on the low performance DELL Latitude E6500 (Intel
 344 Core2 Duo CPU, 2.53 GHz, 4 GB RAM) laptop used here. As expected from the litera-



321 **Figure 7.** (a) and (c): amplitude demodulation, exhibiting dips every second (a) representative of timing
 322 marks (c). (b) and (d): phase cross correlation, again with cross-correlation peaks repeating every second
 323 (b) for a precise time transfer (d). (c) and (d) are zooms on 2.5 s-long parts of the (a) and (b) records. (e) and
 324 (f): comparison of the AM v.s PM cross-correlation timing accuracy by displaying a stack of 20 consecutive
 325 pulses. The Y-axis labeled “xcorr(ph,PRN)” indicates that the magnitude of the cross correlation between the
 326 phase samples and the Pseudo Random Number (PRN) sequence encoding the DCF77 phase is displayed.

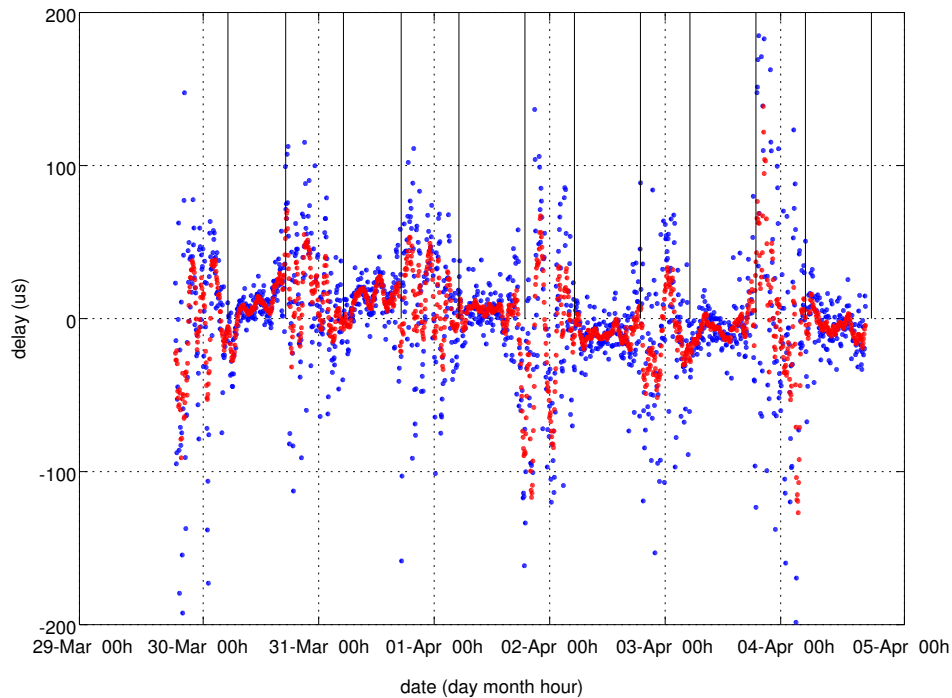
345 ture, the ionosphere is unstable during winter time, with fluctuations in the hundreds of
 346 microsecond range. More interestingly, spring time brings ionosphere stabilization, with a



333 **Figure 8.** Comparison of the time difference between DCF77 and GPS 1 PPS in November (top), as the
 334 ionosphere is not stable during winter, and April (bottom), as the ionosphere stabilizes during daytime in
 335 spring and summer. The red dots represent data resulting from a sliding average over ten samples of the raw
 336 data shown as blue dots, which are themselves measurements integrated over 1 minute intervals (average of
 337 60 DCF77 timing estimates with respect to GPS 1 PPS). All chart abscissa refer to time in UTC, with the date
 338 referring to the 0:00 hour of each day.

347 clear observation of the ionosphere delay stabilization during day time, as the upper layers
 348 of the atmosphere are exposed to solar ionizing radiation particles, and loss of stabiliza-
 349 tion during night. The stabilization matches the sunrise and sunset dates (Fig. 9).

355 Amongst the fascinating consequences of monitoring the LF propagation duration
 356 over a long duration is the hint of some interaction between the upper Earth crust – the
 357 lithosphere – and ionosphere as observed during earthquakes. [*Kumar and Kumar, 2007*;
 358 *Molchanov et al., 1998*; *Chakrabarti et al., 2005*; *Hayakawa et al., 1997*]. The carrier fre-
 359 quency considered here seems to be too high to allow for the observation of cosmic par-
 360 ticle fluctuation as observed from NOAA’s geostationary GOES satellites. Such effects
 361 – Sudden Ionospheric Disturbances (SID) monitoring – is classically performed [*Dolea*



350 **Figure 9.** Short term analysis of the DCF77 timing delay with respect to sunrise and sunset times as calcu-
 351 lated by the USNO application available at http://aa.usno.navy.mil/data/docs/RS_OneYear.php:
 352 the ionospheric delay stabilization when sun rises (vertical lines, alternatively sunset and sunrise time) is
 353 clearly visible in this chart. All chart abscissa refer to time in UTC, with the date referring to the 0:00 hour of
 354 each day.

362 *et al.*, 2013] by observing the *amplitude* variation of the LF signal rather than its time of
 363 flight as considered here.

364 5 Timing accuracy

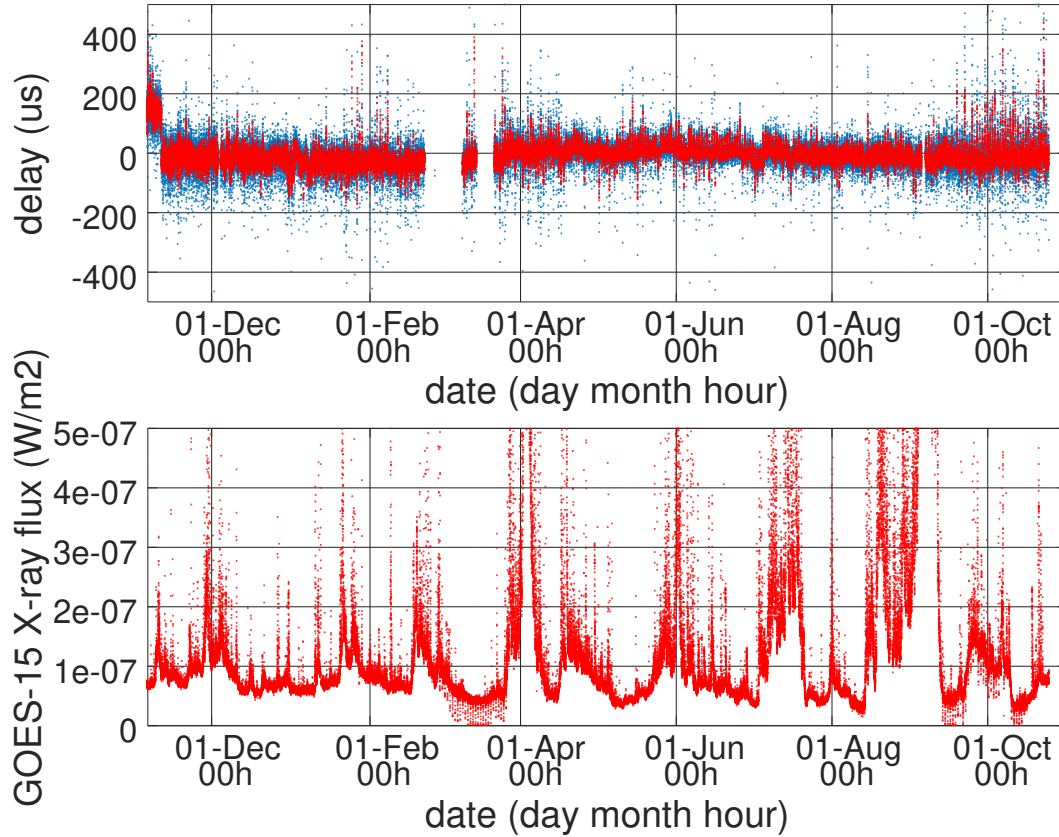
365 A detailed estimate of the accuracy of the time transfer needs to consider the evo-
 366 lution of the offset between GPS 1-PPS and DCF77 (Fig. 10) with integration time. Fur-
 367 thermore, let us remember that the rationale for maintaining VLF timing broadcast sys-
 368 tems such as DCF77 (similar to WWVB in the North America or JJY in Japan) is the
 369 long term synchronization of quartz-controlled clocks whose excellent short term stabil-
 370 ity is given by the resonator but long term stability is poor due to aging, temperature de-
 371 pendence and offset with the nominal frequency with respect to the primary standards:
 372 despite the daily fluctuations of several tens to hundred of microseconds, the long term

373 mean value exhibits no visible drift (Fig. 10, top) despite varying environmental condi-
 374 tions including space weather (Fig. 10, bottom). Controlling the quartz oscillator with a
 375 signal extracted from the VLF timing measurements to generate a stable composite sig-
 376 nal exhibiting the best stability of both systems requires assessing the time constant of the
 377 feedback loop. Such a measurement is classically performed through the Allan deviation
 378 analysis of both clocks: the integration time at which the curves intersect defines the feed-
 379 back loop time constant, as illustrated in Fig. 11.

391 DCF77 measurements are computed every 5 minutes following an integration of
 392 60 pulse timings with respect to GPS 1-PPS. The timing accuracy is hence given by av-
 393 eraging the time offsets normalized to this measurement duration: as an example, a 50 μ s
 394 uncertainty over a 5 minute measurement interval yields a relative accuracy of about $50 \cdot$
 395 $10^{-6}/(5 \times 60) \simeq 2 \times 10^{-7}$. This result is indeed the first value in the Allan deviation
 396 plot exhibited in Fig. 11, in which the $1/\tau$ slope with τ the integration time is observed,
 397 indicating the lack of long term drift and stable time transfer with improved accuracy as
 398 integration time increases. Such a trend contrasts with that of a quartz tuning fork con-
 399 trolled oscillator, which exhibits better short term stability owing to the high quality factor
 400 of the quartz tuning fork, but drifts over long terms to exhibit long term instability greater
 401 than those of the VLF signal. The intersection of the two curves, around 1000-2000 s, de-
 402 fines the feedback loop constant to control the quartz tuning for with the VLF signal. The
 403 proposed setup is hence well suited for a digitally controlled quartz oscillator locked on
 404 the phase information provided by DCF77: we are aware of a single commercial product
 405 implementing such a functionality, namely by Meinberg (Bad Pyrmont, Germany).

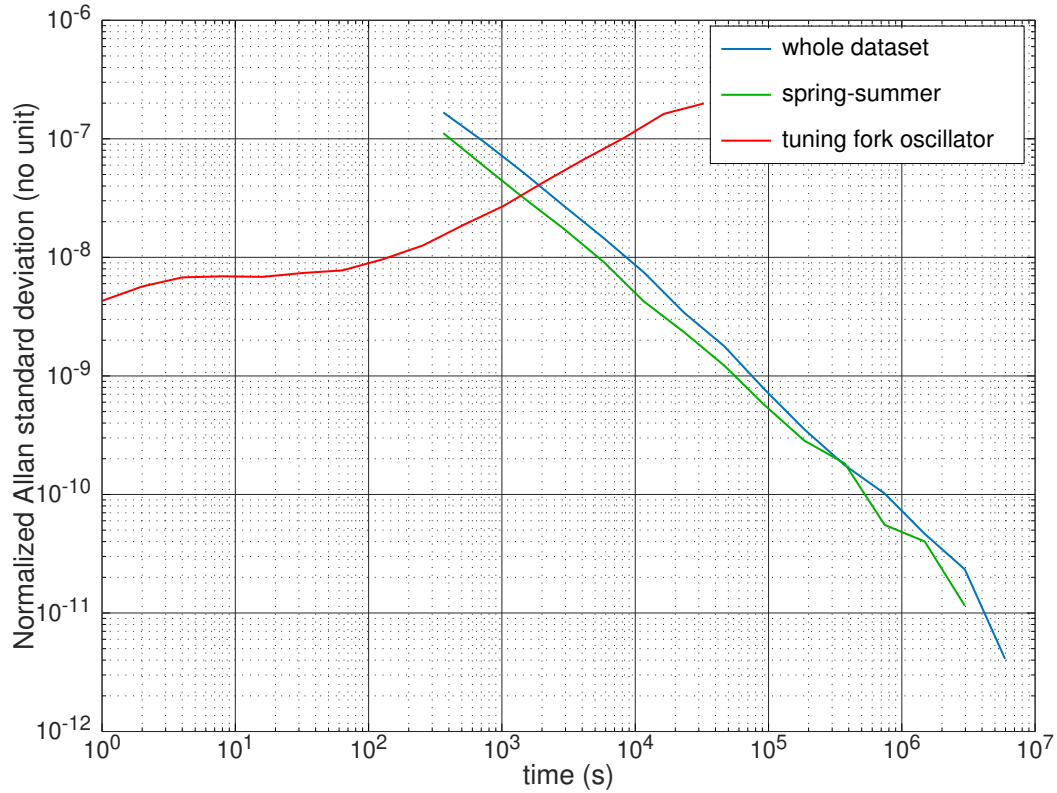
412 **6 Cross-polarization measurements**

413 In a propagating beam model, as opposed to a waveguide model in which the Earth
 414 surface and ionosphere define conducting boundary conditions, the LF wave propagates
 415 along two paths, one along the Earth surface and the other one reflecting on the iono-
 416 sphere. Since the emitter generates a vertically polarized wave and the receiver coil is
 417 horizontal for the magnetic flux to induce a current in each coil, the strongest wave com-
 418 ponent dominates the received signal, making the identification of the wave bouncing off
 419 the ionosphere challenging. Since the wave reaching the ionosphere interacts with an ion-
 420 ized medium with free charges in a magnetic field, polarization rotation occurs through
 421 the Faraday effect, which might provide a solution for separating the air wave from the



380 **Figure 10.** Long term investigation of the delay between the atomic clock-disciplined DCF77 and GPS
 381 1-PPS (top), compared to the X-ray flux observed by NOAA’s GOES geosynchronous satellite observations,
 382 as available from <ftp://ftp.swpc.noaa.gov/pub/lists/xray/> (5 minute interval records from the
 383 primary sensor). No correlation between the two quantities is visible, probably because 77.5 kHz is too high
 384 a frequency to detect such phenomena. The stabilization of the ionospheric propagation properties during
 385 spring and summer are well visible as the reduced fluctuation in the middle part of the top chart (spring and
 386 summer) with respect to the left and right (winter and autumn), with zooms in relevant regions provided in
 387 Fig. 8. The phase jump after the first week of measurement is associated with a slight change in the phase
 388 slope analysis for unwrapping, emphasizing the influence of the signal processing chain on the absolute
 389 phase evaluation. The algorithm was no longer modified after this initial change to ensure continuity of the
 390 measurements. All chart abscissa refer to time in UTC, with the date referring to the 0:00 hour of each day.

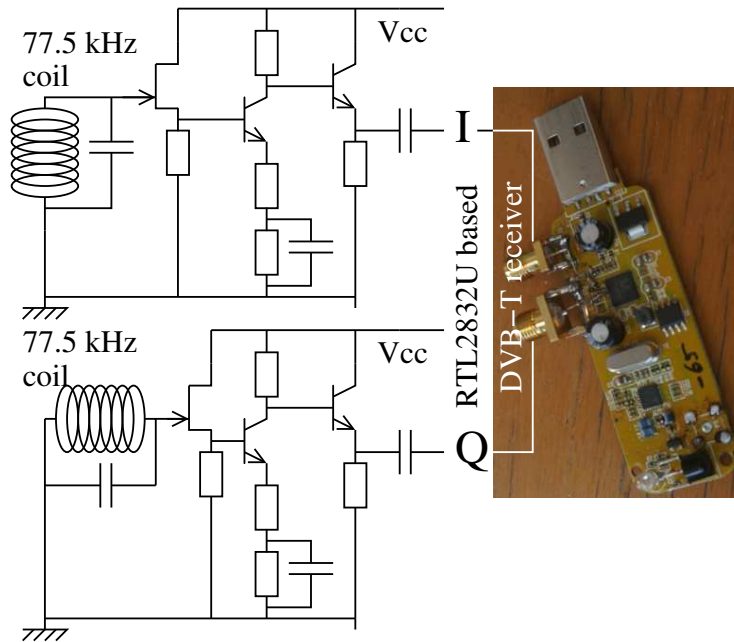
422 ground wave. By performing simultaneously two measurements, one with a horizontal
 423 coil (sensitive to the ground wave – no polarization rotation) and a with a second setup
 424 using a vertically oriented coil (insensitive to the ground wave), the air wave is separated
 425 and the time delay analyzed (Fig. 12). Since an electromagnetic wave propagates with the



406 **Figure 11.** Allan deviation of the time offset between GPS 1-PPS and DCF77 (blue), and of a 32768 Hz
 407 tuning fork oscillator as classically found in wrist watches (red). The intersection of the two curves provides
 408 the time constant of the composite clock in which the DCF77 signal could be fed back to the tuning for os-
 409 cillator to correct long term drift of the latter. The green curve exhibits the Allan deviation of the spring
 410 and summer dataset, starting April 1st, when the ionosphere has stabilized during daytime, improving the time
 411 transfer stability.

426 wavevector \vec{k} , electric field \vec{E} and magnetic field \vec{B} normal to one another, the detected
 427 electric field is along the radius of the coil. Hence, an horizontal ferrite antenna with the
 428 plane containing the coil oriented vertically detects the vertical linearly polarized electric
 429 field, and a vertical ferrite antenna with the plane of the coil horizontal detects the linearly
 430 polarized horizontal electric field.

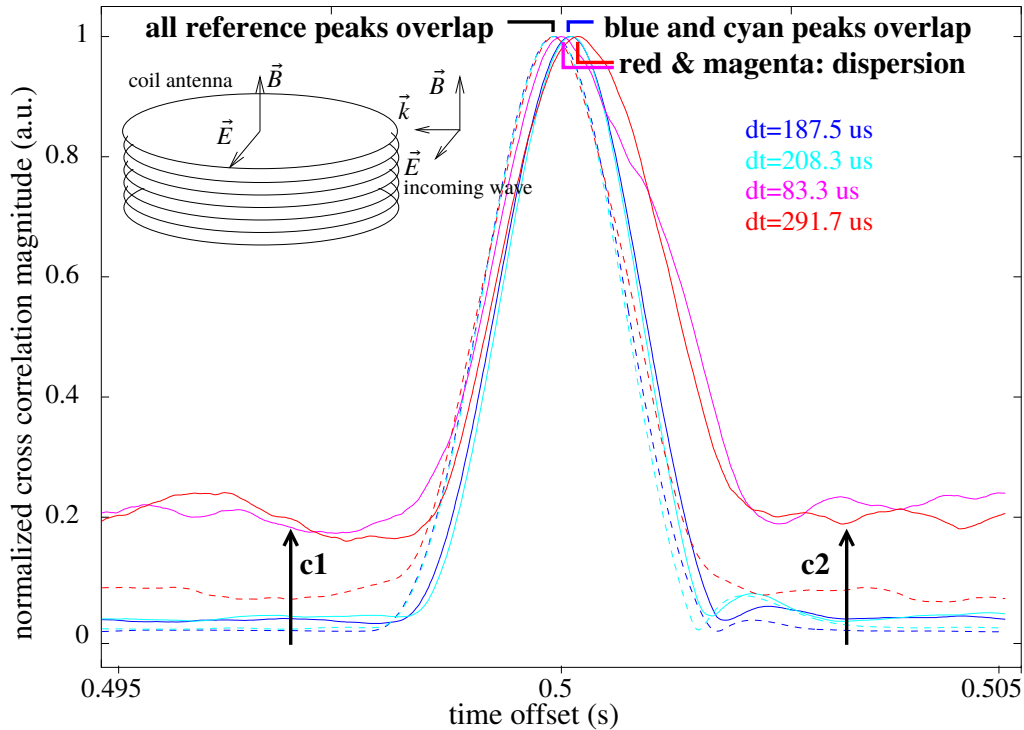
433 In order to reject systematic delay, the setup was rotated 90° half-way during the ex-
 434 periment to check that the delayed channels would switch as the horizontal and vertical
 435 antenna channels were exchanged. Such a result was indeed observed. The mean value of
 436 the delay between the two channels is $170 \pm 60 \mu\text{s}$ (Figs. 13 and 14), surprisingly close to
 437 the expected value deduced from a geometric raytracing model. However, the poor signal



431 **Figure 12.** Crossed polarization measurement: two identical setups are connected to the I and Q inputs of a
 432 RTL2832U based DVB-T receiver.

438 to noise ratio of the vertically polarized antenna prevented identifying day/night fluctu-
 439 ations. Indeed, some negative delay was observed, as opposed to the predicted delay of
 440 the air wave with respect to the ground wave: such measurements were however excluded
 441 following a quantitative criterion of signal to noise ratio on the vertically polarized re-
 442 ceiver. Fig. 13 illustrates this analysis: the selected criterion is inverse of the average of
 443 the two cross-correlation values located at the vertical arrows **c1** and **c2**. Since the cross-
 444 correlation peaks have been normalized, the inverse of the mean value of **c1** and **c2** pro-
 445 vides an indicator of a signal to noise ratio, with measurements rejected if this criterion
 446 is below 15. Each curve set in Fig. 13 includes two traces: one for the horizontal polar-
 447 ization and one for the vertical polarization. Since the horizontal ferrite antenna (vertical
 448 electric field component) always exhibits excellent signal to noise ratio, all curves over-
 449 lap on the left-most reference cross-correlation peak. Poor signal to noise ratio exhibited
 450 by the red and magenta curve yield strong dispersion on the position of the second cross-
 451 correlation peak, while acceptable signal to noise ratio following the proposed criterion
 452 yields to overlapping blue and magenta measurement correlation peaks (right, horizontal
 453 electric field component), allowing for precise time of flight difference measurement with
 454 respect to the reference cross correlation peak (left, vertical electric field component). The

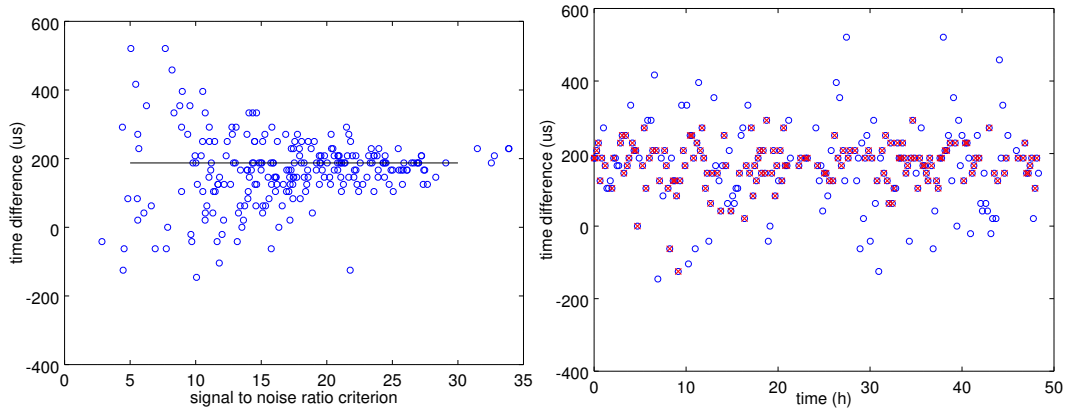
455 values to the right of the graph in Fig. 13 indicate the measured time of flight difference:
 456 the two cases of acceptable signal to noise ratio yield close results of 187 and 200 μs re-
 457 spectively, while the two cases of poor signal to noise ration yield excessively dispersed
 458 results, here 291 and 83 μs respectively.



459 **Figure 13.** Cross-correlation curves for high signal to noise measurements (blue and cyan), and low signal
 460 to noise (red and magenta) ratios. Each dataset exhibits two curves, one for the reference (vertical polarization
 461 – dashed line) and one for the measurement (horizontal polarization – solid line). Signal to noise ratio (SNR)
 462 is defined by the normalized cross correlation peak maximum to the baseline (positions **c1** and **c2**) value.
 463 High SNR yields accurate time delay difference between the vertically (left-most cross-correlation peak) and
 464 horizontally polarized (right-most cross-correlation peak) waves. Inset: the antenna current is generated by
 465 the magnetic flux through the coil.

472 7 Conclusion

473 Software defined radio and digital signal processing are used to analyze a high sta-
 474 bility time and frequency transfer signal emitted at very low frequency by the German
 475 DCF77 emitter. Since the propagation of this signal is dependent on ionospheric condi-
 476 tions and especially the altitude of the layer with the electron density whose plasma fre-



466 **Figure 14.** Crossed polarization measurement: the SNR criterion (left) was applied to reject erroneous
 467 measurements. Right: while all measurements over a two-day period exhibit significant dispersion, primarily
 468 due to the poor SNR of the vertically polarized antenna, selecting the data with a criterion above 15 yields a
 469 time delay between vertically and horizontally polarized signals of $170 \pm 60 \mu\text{s}$ or a median value of $190 \mu\text{s}$.
 470 Blue circles are all the measurements, amongst which only the red crosses meet the criterion defined above
 471 and are considered in the delay calculation.

477 quency matches the radiofrequency wave frequency, the time of flight is representative
 478 of the ionosphere altitude variation. Daily and seasonal variations are readily observed,
 479 thanks to the improved timing capability of the pseudo random phase modulation added
 480 to the coarse amplitude modulation used for time transfer. The temperature dependence of
 481 the local oscillator of the receiver is also observed with this setup, which solely consists
 482 of an antenna, impedance matching circuit and personal computer sound card.

483 Such a basic setup is designed for dissemination and long term monitoring activity
 484 for its low cost and ease of assembly. The performance, allowing for $10 \mu\text{s}$ time of flight
 485 measurement, is suitable for observing daily ionospheric condition variations through tim-
 486 ing analysis rather than the classical amplitude measurement. Daily variations of more
 487 than $100 \mu\text{s}$ are readily observed, as are the seasonal ionosphere stabilization during spring
 488 and summer and instability from the end of autumn to winter. From the authors laboratory
 489 location at a range from the emitter at which the ground wave and air wave exhibit com-
 490 parable amplitude, the vertical (direct) and horizontal (reflected) components of the elec-
 491 tric field exhibit a relative time delay consistent with the expected geometrical model of
 492 wave reflection on the ionosphere.

493 **Acknowledgments**

494 Andreas Bauch (PTB, Germany) prompted this investigation with his course on time trans-
 495 fer at the European Frequency and Time Seminar (efts.eu). Franck Lardet-Vieudrin
 496 (FEMTO-ST, France) provided support in designing and understanding the operating prin-
 497 ciple of the short antenna. François Vernotte (Besançon Observatory, France) provided
 498 the explanation on the conversion of time intervals to normalized quantities for Allan de-
 499 viation analysis. Eric Meyer (Besançon Observatory, France) prompted the investigation
 500 on the cross-polarization time delay measurement. This work was partly supported by
 501 the Programmes d'Investissements d'Avenir (PIA) FirstTF and Oscillator IMP grants. All
 502 datasets are made available to readers at <http://jmfriedt.free.fr/dcf77>.

503 **References**

- 504 ARRL (1997), *ARRL Antenna Handbook, 18th Ed.*, chap. Small Loop Antennas, ARRL.
- 505 Baker, D. N., and L. J. Lanzerotti (2016), Resource letter SW1: Space weather, *American*
 506 *Journal of Physics*.
- 507 Bauch, A., P. Hetzel, and D. Piester (2009), Time and frequency dissemination with
 508 DCF77: From 1959 to 2009 and beyond, *PTB-Mitteilungen*, 119(3), 3–26.
- 509 Blackband, W. (1964), *Propagation of Radio Waves at Frequencies Below 300 Kc*, on behalf
 510 of Advisory Group for Aeronautical Research and Development, North Atlantic Treaty
 511 Organization.
- 512 Carlà, M. (2016), Measure of $1/f$ noise using the sound card of a PC, *American Journal of*
 513 *Physics*, 84(4), 311–316.
- 514 Chakrabarti, S. K., M. Saha, R. Khan, S. Mandal, K. Acharyya, and R. Saha (2005),
 515 Unusual sunset terminator behaviour of VLF signals at 17kHz during the earthquake
 516 episode of Dec., 2004, *Indian J. Radio and Space Phys*, 34, 314–317.
- 517 Davies, K. (1990), *Ionospheric radio*, 31, IET.
- 518 Dolea, P., V. P. Dascal, O. Cristea, and T. Palade (2013), In-situ measurements regarding
 519 If radio wave propagation using DCF77 time signal transmitter, in *Telecommunication in*
 520 *Modern Satellite, Cable and Broadcasting Services (TELSIKS), 2013 11th International*
 521 *Conference on*, vol. 2, pp. 449–452, IEEE.
- 522 Engeler, D. (2012), Performance analysis and receiver architectures of DCF77 radio-
 523 controlled clocks, *IEEE transactions on ultrasonics, ferroelectrics, and frequency control*,
 524 59(5), 869–884.

- 525 Giffard, R. (1999), Estimation of gps ionospheric delay using L1 code and carrier phase
526 observables, in *31st Annual Precise Time and Time Interval (PTTI) Meeting*, pp. 405–
527 416, <http://www.dtic.mil/get-tr-doc/pdf?AD=ADA497270>.
- 528 Gotoh, T., J. Amagai, T. Hobiger, M. Fujieda, and M. Aida (2011), Development of a
529 GPU-based two-way time transfer modem, *IEEE Transactions on Instrumentation and*
530 *Measurement*, 60(7), 2495–2499.
- 531 Hayakawa, M., O. Molchanov, T. Ondoh, and E. Kawai (1997), On the precursory signa-
532 ture of kobe earthquake on VLF subionospheric signals, in *IEEE International Sympo-*
533 *sium on Electromagnetic Compatibility*, pp. 72–75, IEEE.
- 534 Hetzel, P. (1988), Time dissemination via the lf transmitter DCF77 using a pseudo-random
535 phase-shift keying of the carrier, in *Proceedings of the 2nd European Frequency and*
536 *Time Forum (EFTF)*, pp. 351–364.
- 537 Huang, Y.-J., M. Fujieda, H. Takiguchi, W.-H. Tseng, and H.-W. Tsao (2016), Stability
538 improvement of an operational two-way satellite time and frequency transfer system,
539 *Metrologia*, 53(2), 881.
- 540 Johler, J. R. (1962), Propagation of the low-frequency radio signal, *Proceedings of the IRE*,
541 50(4), 404–427.
- 542 Kamp, P.-H. (), A cheap SDR Loran-C frequency receiver, [phk.freebsd.dk/](http://phk.freebsd.dk/AducLoran/AducLoran-0.3.pdf)
543 [AducLoran/AducLoran-0.3.pdf](http://phk.freebsd.dk/AducLoran/AducLoran-0.3.pdf).
- 544 Kumar, S., and A. Kumar (2007), Diurnal variation of 19.8 kHz signal propagation over
545 long path to suva, *The South Pacific Journal of Natural Science*, 11, 67–69.
- 546 Mindell, D. A. (2011), *Digital Apollo: human and machine in spaceflight*, Mit Press, Cam-
547 bridge, MA, USA.
- 548 Mochizuki, K., M. Uchino, and T. Morikawa (2007), Frequency-stability measurement sys-
549 tem using high-speed adcs and digital signal processing, *IEEE Transactions on Instru-*
550 *mentation and Measurement*, 56(5), 1887–1893.
- 551 Molchanov, O., M. Hayakawa, T. Oudoh, and E. Kawai (1998), Precursory effects in the
552 subionospheric VLF signals for the Kobe earthquake, *Physics of the Earth and Planetary*
553 *Interiors*, 105(3), 239–248.
- 554 Piester, D., A. Bauch, J. Becker, and A. Hoppmann (2011), Time and frequency broadcast
555 with DCF77, in *Proc. 43rd Annual Time and Time Interval (PTTI) Systems and Applica-*
556 *tions Meetings*, pp. 185–196.

- 557 Raupach, S. M., and G. Grosche (2014), Chirped frequency transfer: a tool for synchro-
 558 nization and time transfer, *IEEE transactions on ultrasonics, ferroelectrics, and frequency*
 559 *control*, 61(6), 920–929.
- 560 Schulte, C. H., G. M. Müller, H. Horn, J. Hübner, and M. Oestreich (2012), Analyzing
 561 atomic noise with a consumer sound card, *American Journal of Physics*, 80(3), 240–245.
- 562 Sherman, J. A., and R. Jördens (2016), Oscillator metrology with software defined radio,
 563 *Review of Scientific Instruments*, 87(5), 054,711.
- 564 Uchino, M., and K. Mochizuki (2004), Frequency stability measuring technique using dig-
 565 ital signal processing, *Electronics and Communications in Japan (Part I: Communica-*
 566 *tions)*, 87(1), 21–33.
- 567 Watt, A., R. Plush, I. Brown, and A. Morgan (1972), Worldwide VLF standard frequency
 568 and time signal broadcasting, *Precision Measurement and Calibration*, 5, 297.

569 **A: GNU/Octave implementation of the decoding sequence**

```
570 x=read_complex_binary(d);
571 dcf=real(x);
572 gps=imag(x);
573 fs=192e3;
574 time=[0:length(x)-1]/fs;          % fs = sampling rate
```

575 The file named `d`, created by GNURadio as a binary record with floating point for-
 576 mat alternating the left and right audio channels, recording the DCF77 antenna output and
 577 GPS 1 PPS signal respectively, is read and the time index is created with steps given by
 578 the inverse of the sampling rate `fs`.

```
579 dcf=dcf.*exp(j*2*pi*(77500)*time);
580 lpf=firls(250,[0 720 790 fe/2]*2/fe,[1 1 0 0]);
581 dcf=filter(lpf,1,dcf);
582 x=dcf(1:59:end);
583 time=time(1:59:end);
```

584 The signal is transposed from radiofrequency band (77.5 kHz) to baseband by a
 585 multiplication with the local oscillator synthesized digitally as a sine wave with angular
 586 pulsation $2\pi \times 77500$ rad/s. The low-pass filter removes noise and unwanted parasitic

587 components from the mixing step: indeed, the magnitude of the Fourier transform of the
 588 real signal dcf77 is even, and the frequency transposition creates a spectral component
 589 at $-77.5-77.5=-150$ kHz which is aliased to $192-150=42$ kHz, eliminated by the low-pass
 590 filter. Once the signal is brought to baseband, the whole bandwidth is no longer needed
 591 since the signal is only located a few kHz around baseband: excess samples are discarded
 592 by decimating by 59, and time is decimated similarly, equivalent to dividing the sampling
 593 rate by this same factor. The decimation factor of 59 was selected considering the known
 594 bit-rate of the signal emitted by DCF77, namely 120 periods of the 77500 Hz carrier, or
 595 1.5484 ms. The decimation factor of 59 was selected to have a small integer number of
 596 samples during each bit: $59/192 = 0.3073$ ms which is $1.5484/0.3073 = 5.04$ close
 597 to 5 samples/bit. Such a selection will make the cross-correlation with a pseudo-random
 598 code re-sampled to the selected sampling rate easier to analyze.

```
599 [yf,xf]=max(abs(fft(x-mean(x))))); % coarse frequency offset identification
600 xf=xf-length(x)-1;
601 df=-xf/length(x)*fs % index to frequency conversion
602 lo=exp(j*2*pi*df*time); % transpose by xf (fe->fe+xf ou fDCF->fDCF-xf)
603 x=x.*lo;
```

604 Following the transposition from radiofrequency band to baseband by the nominal
 605 frequency offset, a fine tuning of the difference between the local oscillator frequency and
 606 remote oscillator frequency is identified as the frequency at which the Fourier transform is
 607 maximum. This Fourier transform index is converted to a frequency by remembering that
 608 a discrete Fourier transform over N samples spans from minus half of the sampling fre-
 609 quency to half of the sampling frequency, or a bin size of fs/N . Again the multiplication
 610 brings the signal exactly on the baseband 0-Hz frequency.

```
611 [u,v]=polyfit(time,xp,1); % once coarse offset removed, linear fit on phase
612 x=x.*exp(-j*time*u(1)-j*u(2)); % linear phase shift = frequency offset
613 xp=angle(x); % phase modulation ...
```

614 Since we aim at demodulating a phase-modulation, any leftover phase drift must be
 615 removed. The frequency is the derivate of the phase, so that the previous step might have
 616 left a fine phase drift with a slope below the bin size of the Fourier transform: a linear
 617 polynomial fit gets rid of the fine linear drift, or residual frequency offset. These last fine-

618 tuning steps must be repeated for each new record since the local oscillator frequency,
619 clocking the sound card, fluctuates over time with environment (Fig. 6).

```
620 load lfsr.dat
621 np=192000/59*(120/77500);          % PRN chip length (120 periods of carrier)
622 oldP=0;
623 for k=1:length(lfsr)
624     P=round(k*np);                % resample
625     if (lfsr(k)==1) longlfsr(oldP+1:P)=ones(P-oldP,1);
626     else longlfsr(oldP+1:P)=zeros(P-oldP,1);
627     endif
628     oldP=P;
629 end
```

630 Having recovered a fine estimate of the received signal phase, we aim at extract-
631 ing the pseudo-random phase sequence imprinted on the carrier. The bit-sequence gen-
632 erated by the polynomial was computed and stored in a `lfsr.dat` file as described in
633 section 3, with a rate of 1 sample/state. The sampling rate resulting from the decima-
634 tion was selected to have a number of samples of the phase close to an integer number
635 of samples of the phase encoding: at 120 periods/phase state, the number `np` of sam-
636 ples is $192000/59 \times (120/77500) = 5.04$, close enough to 5 for the 512 sample long
637 pseudo-random code to be easily re-sampled to match the current sampling rate: each bit
638 is copied enough time for the sampling rates to match, resulting in the `longlfsr` vector.

```
639 yc=xcorr(xp-mean(xp),longlfsr-mean(longlfsr));
640 yc=yc(floor(length(yc)/2):end); % cross correlation result
```

641 Finally, the cross-correlation between the phase `xp` and the pseudo-random sequence
642 `longlfsr` is computed, having previously removed the mean value of each signal to pre-
643 vent a triangular baseline variation due to the integral over a constant offset: the cross-
644 correlation `yc` exhibits maxima